



In situ monitoring of build height during powder-based laser metal deposition

Jiayu Ye^{1,2} · Nazmul Alam¹ · Alejandro Vargas-Uscategui¹ · Milan Patel² · Alireza Bab-Hadiashar² · Reza Hoseinnezhad² · Ivan Cole²

Received: 13 May 2022 / Accepted: 9 September 2022 / Published online: 16 September 2022
© The Author(s) 2022

Abstract

A powder-based laser metal deposition (LMD) system can fabricate customised three-dimensional (3D) parts, layer by layer, based upon a computer-aided design (CAD) model. However, the deposition will not always feature the expected geometry due to excessive heat input and inconsistent powder flow. Due to the layer-by-layer nature of LMD, geometrical error in one layer is compounded in all following layers and may result in a build failure. Thus, it is critical to monitor online the track and layer height. This study developed an in situ monitoring system integrating a webcam and a narrow bandpass filter. The laser/powder defocus distance was extracted from the melt pool images, and the track/layer height was calculated from the laser/powder defocusing distance and preprogrammed layer spacing. The presented approach does not need additional illumination sources and is a nonintrusive online method. Therefore, it is a potential precursor to a feedback build height control system. It also can be used for measuring omnidirectional height, i.e. height in different build directions relative to the substrate, which has been tested by fabricating two thin-wall structures with customised shapes. These online-measured height data were successfully validated against dimensional measurements from an offline 3D scanner, thus demonstrating the online system's potential utility in a feedback control system for ensuring acceptable part geometrical accuracy.

Keywords Laser metal deposition (LMD) · In situ monitoring · Image processing · Height measurement

1 Introduction

LMD is a metal-based additive manufacturing method [1] and is particularly competitive in achieving a high mass deposition rate and building flexibility. As a result, it is widely applied to the fabrication of customised 3D parts and part repair in the aviation, automotive, and biomedical sectors [2]. Metal powder or wire is fed to a region of the substrate surface (i.e. the melt pool) being melted by a moving laser beam. The feed material is melted within the melt pool and resolidified after the laser leaves the area. The laser path is carefully preprogrammed to generate deposition tracks in a track-by-track and layer-by-layer manner to deliver the desired component geometry [3].

Despite its ability to manufacture components with complex 3D geometry, powder-based LMD-manufactured builds still face quality issues, particularly nonuniform build geometry (particularly build height), even for a constant preprogrammed laser path and (other) process parameters. Three main factors affect the delivery of correct build geometry, namely.

1. Even for constant-valued process parameters, fluctuation still occurs in, e.g. powder feed rate, due to variation in incoming powder flow rate, resulting in uneven build height. The laser beam and powder jet become mutually defocused at convex (overly large build height) and concave positions (overly small build height). These build height errors propagate to subsequent layers and can significantly distort parts.
2. An uneven substrate surface will also affect overall build height, typically not compensated for during laser path planning.
3. During trajectory changes, the laser's acceleration and deceleration affect the amount of powder caught by the melt pool, affecting the overall build height [4, 5].

✉ Jiayu Ye
jiayu.ye@student.rmit.edu.au

¹ CSIRO Manufacturing, Normanby Road, Clayton, VIC 3168, Australia

² School of Engineering, RMIT University, Melbourne, VIC 3000, Australia

This study focuses mainly on the online measurement of build height via in situ monitoring of the laser/powder defocusing distance to develop a precursor for a feedback control system for build height for LMD printers. In situ monitoring of an uneven substrate surface is briefly discussed but is not the current focus, as is neither laser acceleration nor deceleration.

The effect of the laser/powder defocusing distance on thin-wall structures was studied for single-track builds and reported elsewhere [5]. The largest single-track height obtained in this prior study occurred when the powder jet's focal plane was aligned to the melt pool and decreased when the powder focus moved above or below. However, the study concludes that the thin-wall build achieved better geometrical accuracy when the powder focal plane was slightly below the substrate plane. The preprogrammed layer spacing (Δz) in the laser's toolpath program also affects the laser/powder defocusing distance. The relationship between laser/powder defocusing distance and cladding layer height was reported in [1] and concluded that the layer spacing (Δz) should be kept in a suitable range of 0.4–0.7 times the cladding layer height for obtaining good part quality. However, even with such static optimisations to Δz [6–8], as long as the LMD system is running in an open-loop manner, the fabrication process is still not robust to disturbances (e.g. fluctuation of powder feed rate due to online variation in powder size), which therefore still leads to dimensional inaccuracy [9].

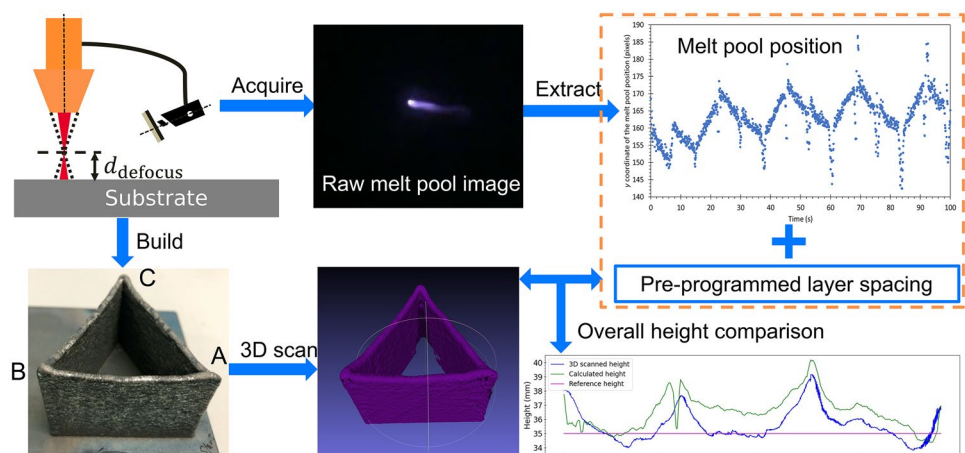
Before designing a feedback controller for layer height for the LMD process, it is necessary to acquire an in situ measured signal that reflects the build height accurately. Several articles have reported such techniques, e.g. via a 3D scanner or a LDS mounted off-axially to the laser-powder feed system [4, 9–11]. These systems are typically precise to micron-scale and scan the build after each layer is deposited to obtain a complete layer height profile. Thus, these methods introduce an interlayer pause, periodically interrupting and slowing the fabrication process. Moreover,

interruptions can result in a coarser build surface and even cracks [12]. Triangulation methods for height monitoring have also been proposed by integrating camera(s) off-axially to the laser-powder feed system [13–17] or coaxially [18, 19]. Compared to the scan-based method, off-axially integrated cameras have the advantage of not disturbing the laser by height measurement and (thus) real-time monitoring of build height. However, camera-based height measurement methods usually require high-quality images that require additional illumination and limited installation locations.

This study proposes a low-cost solution for in situ monitoring of build height, based on off-axially mounting a webcam and a narrow bandpass filter; see Fig. 1. Melt pool images are acquired from the webcam and processed using an adaptive thresholding method to estimate the location of the melt pool's centre. The laser/powder defocusing distance can be extracted from the melt pool position. The build's height can, in turn, be calculated based on the preprogrammed Δz and the extracted laser/powder defocusing distance. This calculated build height is compared to offline height profiles obtained from the finished build's 3D scanned point cloud data. The error between calculated height and measured height was found to lie within a reasonable range compared to the existing literature [14]. The results presented here thus prove the feasibility of implementing an off-axial camera to monitor build height online during continuous LMD. This information can then be used within a control system for delivering accurate build height during LMD.

The advantages of the presented in situ monitoring system are as follows: (1) The presented in situ monitoring system is simple, as it consists of one only camera, one narrow bandpass filter, and one cover slide. There are no other cameras (i.e. as for the trinocular-based method [13, 17]) or illumination/probe sources needed, i.e. as in [14, 18, 19]. (2) As the camera was off-axially mounted on the laser head, it moved with the laser head during deposition.

Fig. 1 Schematic workflow used in the present study



The presented approach can thus be used without stopping the process, e.g. unlike scanner-based monitoring systems [10, 11, 20]. 3) The presented approach has been tested by measuring the overall height of customised-shape samples, which reveals that it can successfully measure omnidirectional heights, i.e. in build directions non-perpendicular to the substrate. In contrast, most publication reviewed here tested their methods solely using single-track thin wall fabrication [9, 14].

2 Methods and materials

2.1 Experimental setup

The LMD system consisted of a 4 kW diode laser generator (LDF 4000–100, Laserline GmbH, Mülheim-Kärlich, Germany), a 0.6 mm diameter optical transmission fibre attached to the laser generator that worked in continuous wavelength mode (980–1030 nm), a 6-axis robotic arm (IRB2400, ABB Ltd, Zürich, Switzerland), a laser head attached to the end of the robotic arm, and a powder feeder system (Metco Twin 10-C, Sulzer Ltd, Winterthur, Switzerland). The laser head was equipped with a collimating lens (72 mm focal length) and focusing lens (300 mm focal length) to form a 2.5 mm diameter laser beam with a ‘top hat’ (or rectangular function) intensity distribution.

The laser beam and powder jets were set to focus at the same horizontal plane—the definition of the laser/powder defocusing distance (d_{defocus}) is presented in Fig. 2. A consumer range webcam [21] (LifeCam Cinema, Microsoft Corporation, Redmond, Washington, USA) was mounted upon the laser head in an off-axial position, $\sim 70^\circ$ to the vertical direction and 150 mm horizontally away from the laser head (Fig. 2). A low-cost narrow bandpass filter [22] (20BPF10-900, MKS Instruments, Inc., Andover, Massachusetts, USA) was placed in front of the webcam to monitor the melt pool by permitting only a narrow spectral band of near-infrared (central wavelength 900 nm, full-width half max 10 ± 2 nm).

A disposable transparent cover slide was mounted in front of the bandpass filter for protection purposes.

The optimum angle and distance between the camera and laser head were determined empirically. While their exact values are not critical, several guiding principles must be considered during selection. The angle cannot be too small (e.g. 0°) as the acquired images would show the melt pool in plan view, thus obscuring measurements of d_{defocus} . The angle cannot be too large (i.e. near 90°) as the camera’s view melt pool may be blocked by the height variations elsewhere along the track, particularly when used for omnidirectional height measurement, i.e. for build directions non-perpendicular to the substrate. The distance between the camera and laser head should be neither too small (heat conduction damages the camera) nor too large (decreased image resolution).

2.2 Materials

Commercial stainless steel (SS) 316L powder (SS316L-5320, Höganäs AB, Höganäs, Sweden) was used for all builds described in this study. The as-received particle size was in the range of 45–150 μm . Figure 3a presents a scanning electron microscope (SEM) image of the particles and their particle size distribution. The particles were heterogeneous, with their modal size bin at 71–106 μm as measured from SEM images (Fig. 3b). Regarding the substrate, rectangular mild steel plates ($150 \times 100 \times 10$ mm³) were selected for all builds.

2.3 Camera calibration

As the camera was mounted on the laser head, it moved simultaneously. Thus, the melt pool should appear stationary within the acquired images, provided no laser/powder defocus. Once defocusing occurs, the melt pool changes in a vertical position relative to the camera, manifesting as a change in its apparent size within the image. This effect permitted a calibration experiment to be conducted to determine the effective image resolution of the camera for height measurement. The laser was deliberately moved

Fig. 2 Schematic of experimental setup used for height monitoring

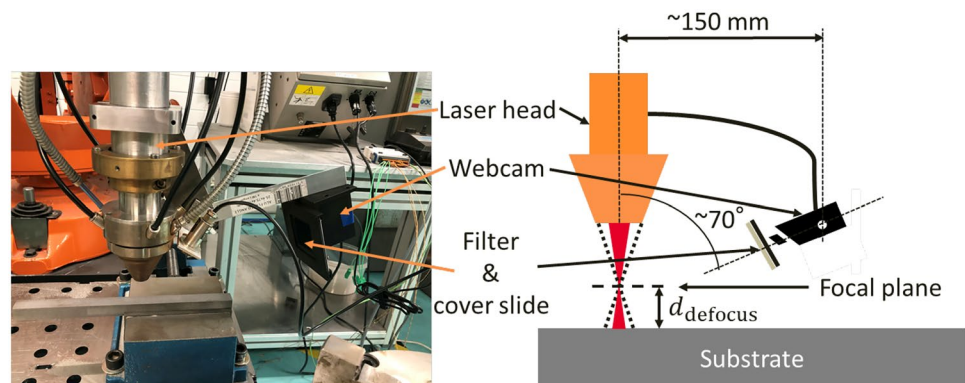
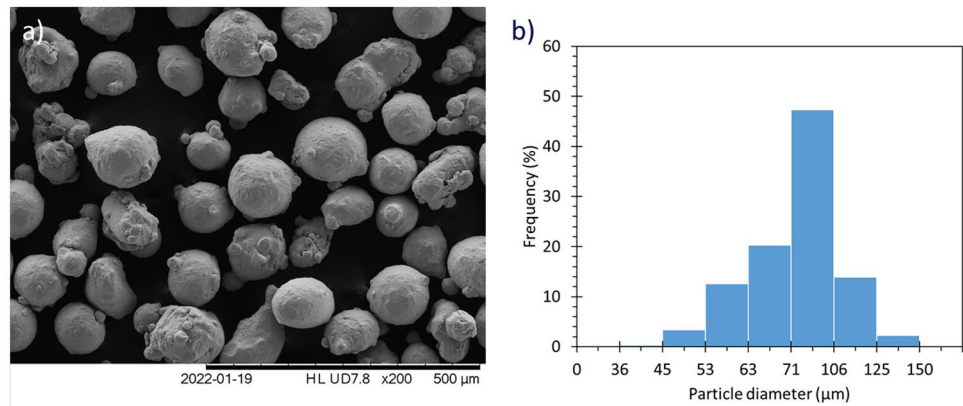


Fig. 3 **a** SEM image of SS316L powder used for all builds described in this study and **b** corresponding particle size distribution, which is adapted from the vendor's datasheet and very similar to that obtained from the SEM images (not included for brevity)



from a focal plane 10 mm above the substrate top surface to a second plane 10 mm below; see Fig. 4.

The laser was switched on without powder flow throughout this movement, and the evolution of melt pool size with laser head distance was recorded. Specifically, the melt pool was detected and extracted from each image using the Otsu adaptive thresholding method [23] included within the OpenCV-Python v4.5.3.36 library (henceforth abbreviated to 'OpenCV'). The melt pool's boundary was then extracted and fitted with an ellipse. The relative y -coordinate of the ellipse centre was then extracted from the processed images and scaled to lie within $[-10, +10]$ mm. The results are highly linear (Fig. 5) and permit the camera's effective image resolution (d_{res}) to be calculated as 0.42 mm/pixel (2 significant figures–SF).

2.4 Image processing and height calculation

As the LMD process builds parts in a layer-by-layer manner, the user may naively expect the deposition height to match the preprogrammed layer spacing/thickness, thus obtaining a part geometry consistent with the simple virtual slicing of its designed geometry. However, due to the high-velocity

fluid dynamics of the melt pool and unavoidable residual fluctuations in controlled process parameters, it is difficult to achieve a perfectly consistent deposited geometry.

When depositing a new layer atop its preceding layer, the laser beam and powder jet defocus at convex positions (i.e. relatively high positions) of the previous layer and similarly at concave positions (i.e. relatively low positions) of the previous layer. Within a limited range of $d_{defocus}$, relatively small convex and concave regions of the preceding layer are compensated during the deposition of successive layers by the self-healing or self-regulation effect [5, 16, 24]. Thus, minor instances of defocusing may not lead to the part fabrication failure, but they still affect the part geometry. The deposition height monitoring system proposed here takes advantage of this behaviour, i.e. instead of monitoring deposition height directly, the laser/powder defocusing distance is observed instead, with the build height $h(t)$ calculated via Eq. (1), where $d_{defocus}$ represents the laser/powder defocusing distance, t represents time, n represents layer number, and Δz represents the preprogrammed layer spacing:

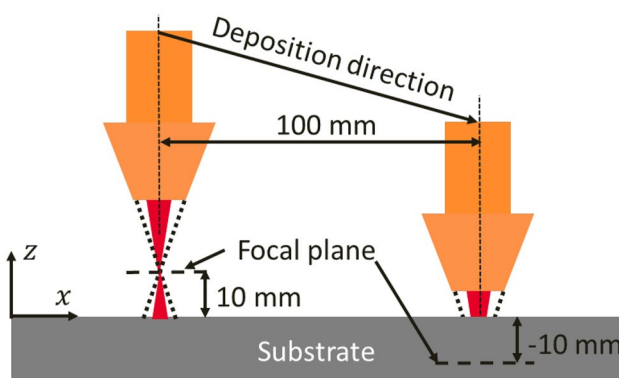


Fig. 4 Schematic of laser head movement during the camera resolution calibration experiment

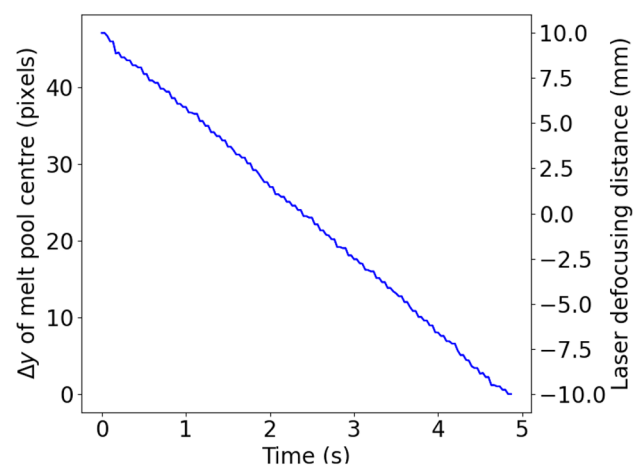


Fig. 5 Results obtained during calibration of the camera used for imaging the melt pool during all experiments conducted in this study. The changing y -coordinate of the melt pool centre was manually scaled to lie within $[-10, +10]$ mm

$$h(t) = d_{\text{defocus}}(t) + n\Delta z, \quad n = 2, 3, 4 \dots \quad (1)$$

d_{defocus} for the n th layer is calculated via Eq. (2), where y_{centre} represents the y -coordinate (in pixels) of the centre of the melt pool’s fitted ellipse, and d_{res} represents the image resolution:

$$d_{\text{defocus}}(t) = (y_{\text{centre}}^n(t) - y_{\text{centre}}^1(t)) \times d_{\text{res}}, \quad n = 2, 3, 4 \dots \quad (2)$$

Two challenges must be addressed to extract robustly y_{centre} from the melt pool images when processing the melt pool images of thin-wall structures. Firstly, as the webcam does not have zoom functionality, the melt pool occupies only a small proportion of its images, and the ellipse fitting will sometimes fail to identify y_{centre} ; see Fig. 6a. Secondly, when printing thin-wall structures, the melt pool tail (Fig. 6b) increases in length and width as heat accumulates with successive layers. These challenges affect the accuracy of the algorithm for locating y_{centre} as well as the calculation of d_{defocus} if using just a singly run thresholding method to extract the melt pool boundary.

This study presents an adaptive thresholding method to address both the above challenges, thus improving the robustness of the image processing algorithm for identifying the y -coordinate (in pixels) of the centre of the melt pool’s fitted ellipse (y_{centre}); see Fig. 7. When a raw image is supplied, the region of interest (ROI) is cropped from the raw image. This ROI is zoomed to $5\times$ larger while maintaining apparent resolution using bicubic interpolation [25]. This zooming and interpolation prevent the failure of the automated melt pool boundary detection and ellipse fitting code by refining the apparent image resolution to 0.084 mm/pixel. This refined image is then binarized using an initial threshold suggested by the Otsu adaptive thresholding method within OpenCV for the analysed image set. Each binarized image is fitted with an ellipse outline via a preexisting OpenCV function [26]. If the major axis a of the ellipse is shorter than an empirical value ‘ l ’, $y_{\text{centre}}^n(t)$ was stored. If $a \geq l$, the minimum threshold limit is increased by unity and the thresholding, binarization, and ellipse-fitting steps

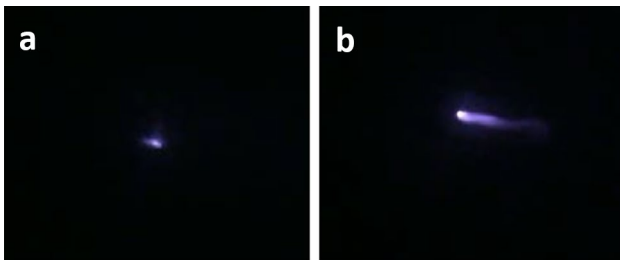


Fig. 6 **a** Example of a melt pool image that usually occurs at the beginning of the printing process. **b** Example of a melt pool image that usually occurs after a couple of layers are printed

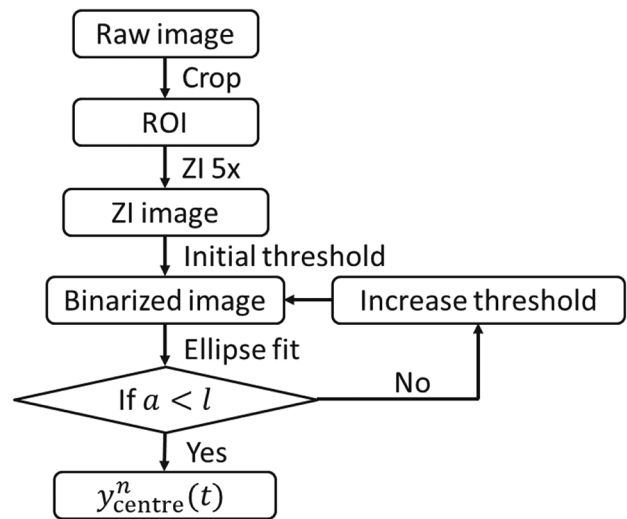


Fig. 7 Workflow for determining the y -coordinate of the centre of the melt pool within camera images taken during real part printing. ‘ZI’ refers to the associated image being both zoomed into the ROI and interpolated to increase its apparent resolution (Sect. 2.4)

are rerun. This process is rerun until a meets the constraint above. The overall process described in Fig. 7 thus eliminates the undesirable inclusion of the melt pool tail within the melt pool boundary, and therefore the associated error during the determination of the y -coordinate (in pixels) of the centre of the melt pool’s fitted ellipse (y_{centre}).

3 Results

A triangle-shaped and an arrow-shaped thin-wall structure were built in continuous mode to test the in situ build height monitoring method presented here. The off-axial camera recorded the fabrication process during both builds. The process parameters for both builds are listed in Table 1. The parameter values were determined empirically from the authors’ lab database of single-track builds using SS316L powder.

3.1 Case study–triangle-shaped thin wall build

Figure 8a presents a photograph of this build. The plan view describes an isosceles triangle with a 50 mm bottom

Table 1 Process parameters used to print two thin-wall structures to validate the proposed method of build height monitoring

Laser power (W)	Scanning speed (mm/s)	Powder feed rate (g/min)	Δz (mm)	Layer number
1500 ± 1	10 ± 1	24.86 ± 0.01	0.7 ± 0.1	50

edge and 60 mm height. The shape of the as-built part was measured to ± 0.02 mm using a portable 3D scanner (HandyScan3D, Creaform, Levis, Canada); see Fig. 8b. The scan results were processed, and the built height along the wall's upper edge was extracted using open-source software (MeshLab 2020.12); see Fig. 8c, d. The scan path in Fig. 8c follows the laser-bearing robot's tool path. v represents the laser scanning speed. Figure 8d presents the comparison between the height profile of the completed build's upper edge from the 3D scanner (h_{scan}), vs. the calculated height based on Eq. (1) (h_{cal}), and the design height based on the preprogrammed layer spacing multiplied by the layer number (h_{ref}). h_{cal} was filtered using a 5-point moving average to improve clarity. Note that as the length of h_{cal} and h_{scan} are different, Eq. (3) cannot be implemented directly, and linear

interpolation was applied via the 'scipy.interpolate' [27] function to artificially equate the lengths of h_{cal} and h_{scan} .

The completed build's heights for positions A, B, and C were marked as dark blue crosses and, while near-symmetric around the isosceles triangle's symmetry plane, exceeded the mid-side heights. This result was due to the deceleration and acceleration of the laser's robotic arm as it approaches and leaves the corner positions, respectively, which results in greater heat build-up, a larger melt pool, greater powder capture, and a higher build-up rate. The error percentage ' δ ' was calculated using Eq. (3) and presented in Fig. 8e, where h is the expected value of the built height and \hat{h} is the built height calculated after the image processing steps described in Sect. 2.4. The yellow line shows the δ between h_{cal} and h_{ref} and the cyan line shows the δ between h_{cal} and h_{scan} .

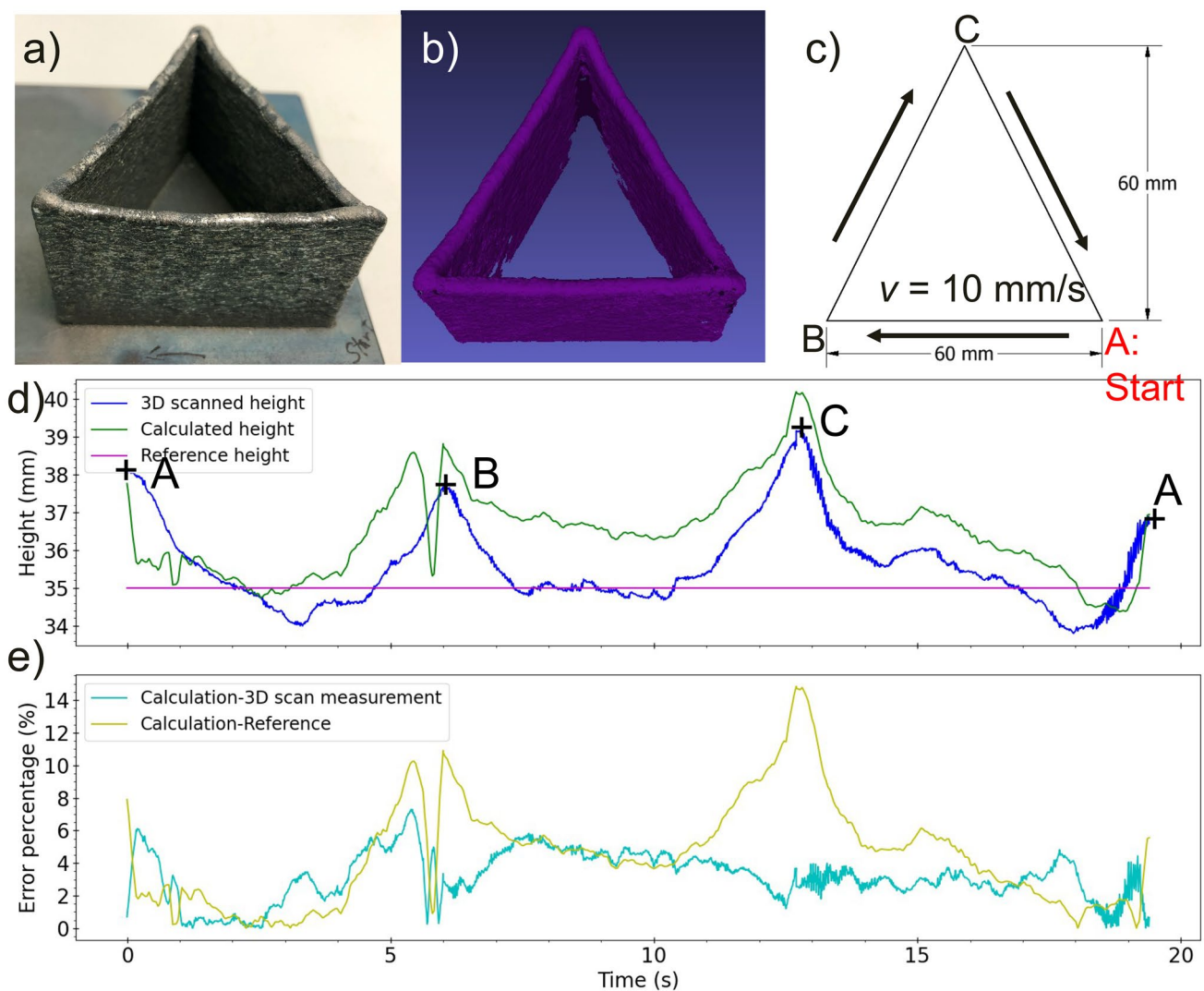


Fig. 8 Results for a triangle-shaped thin wall build. **a** Photograph of the completed build. **b** 3D scanned surface of (a). **c** Plan view of the tool path used by the laser's robotic arm to build (a); note that v is the robot's speed. **d** Comparison between the 3D scanned height (h_{scan}),

calculated height (h_{cal}) via Eq. (1), and the design height (h_{ref}). The heights of positions A, B, and C for the completed build are marked with dark blue crosses. **e** Discrepancy percentages for h_{cal} relative to h_{scan} and h_{cal} relative to h_{ref}

Table 2 Error measures between the calculated overall triangle-shaped thin wall height (after all image processing steps described in Sect. 2.4) and both the overall reference height and 3D scanned overall height. MAE and MXAE are precise to ±0.01 mm, while MAPE and MXAPE are precise at 0.01%

Similarity of different height measures (\hat{h}, h)	MAE (mm)	MAPE (%)	MXAE (mm)	MXAPE (%)
h_{cal}, h_{ref}	1.57	4.49	5.19	14.84
h_{cal}, h_{scan}	1.13	3.17	2.62	7.29

Four error evaluations were obtained from Fig. 8d and e and are presented in Table 2. These include the mean absolute error (MAE), maximum absolute error (MXAE), mean absolute percent error (MAPE), and maximum absolute percent error (MXAPE); see Eqs. (4)–(7), where m is the length of the variable arrays.

$$\delta = \frac{|h - \hat{h}|}{h} \times 100\% \tag{3}$$

$$MAE = \frac{1}{m} \sum_{i=1}^m |h_i - \hat{h}_i| \tag{4}$$

$$MXAE = \max\{x : x \in MAE\} \tag{5}$$

$$MAPE = \frac{1}{m} \sum_{i=1}^m \frac{|h_i - \hat{h}_i|}{h_i} \times 100\% \tag{6}$$

$$MXAPE = \max\{x : x \in MAPE\} \tag{7}$$

The MAE and MXAE between h_{cal} and h_{ref} were 4.49% of MAPE and 14.84% of MXAPE, respectively. These relatively high absolute errors appear due to the aforementioned deceleration and acceleration of the laser’s robotic arm at the build’s corners, e.g. the peaks in δ in Fig. 8e near A and B. This may be related to errors in y_{centre} -determination during image processing; when the laser beam passes the corners, especially for the last layer, the uneven surface at the corner may block the view of the melt pool. Thus, the camera would see only the portion of the tail up to the highest point of the wall, i.e. the preceding build corner. This would result in an abnormal y_{centre} value that affects the accuracy of the h_{cal} values calculated using Eq. (1). The MAE between h_{cal} and h_{scan} was 1.13 mm, which is below the MAE between h_{cal} and h_{ref} , and the MXAE between h_{cal} and h_{scan} was 2.62 mm. The MAPE and MXAPE between h_{cal} and h_{scan} are 3.17 and 7.12 < 10%, respectively, which are both acceptably low [28] and even slightly closer to as-built values than the results presented by [14].

The y_{centre} vs. historical time profile extracted from the melt pool images is presented in Fig. 9, with the initial and final

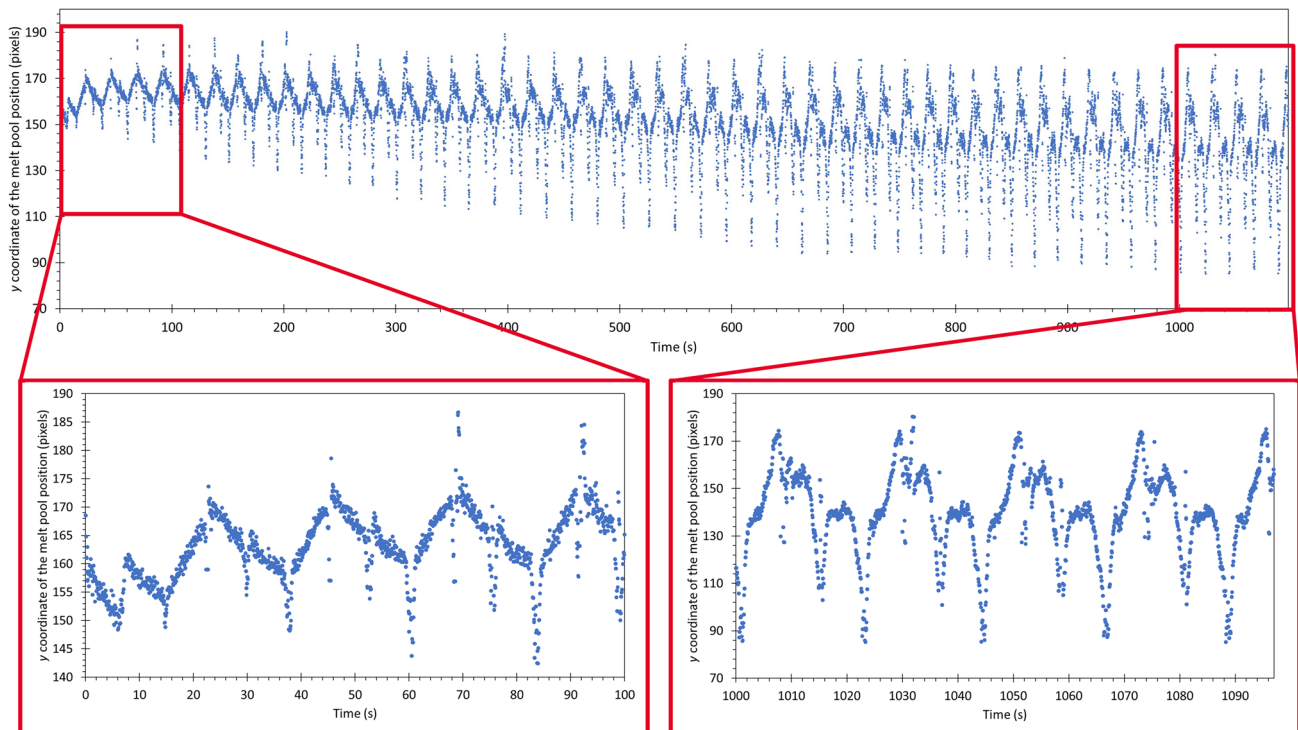


Fig. 9 y -coordinate of the melt pool centre (y_{centre}) as extracted from the melt pool images in a triangle-shaped thin wall build. The initial and final 100 s of the fabrication process were magnified for clarity

periods of the 100 s build magnified for clarity. The y_{centre} of each edge can be distinguished as they have similar patterns that are repeated in the zoomed-in plots. The major peaks and valleys represent the corners and mid-sides of the triangle, respectively. The y_{centre} of each edge in the initial depositing period is quasi-linear, which represents the height of each edge as linearly changing. The y_{centre} for each edge in the final depositing period appears to ‘vibrate’, which represents the height profile of each edge as oscillating. Interestingly, for the first build layer, instead of y_{centre} lying within a horizontal plane, y_{centre} varied in vertical position quasi-linearly with laser displacement for each edge of the triangle. This is likely because the substrate plate’s surface is not flat (see Appendix for evidence).

3.2 Case study–arrow-shaped thin wall build

An arrow-shaped thin wall build (Fig. 10a) was fabricated to test the height monitoring method’s feasibility. Its plan-view

dimensions are $\sim 100 \times 80 \text{ mm}^2$. The scan path in Fig. 10c was built by setting the laser robot’s tool path to follow the scan path clockwise through positions A–B–C–D–E–F–G–A. The y_{centre} vs. time profile extracted from the resulting melt pool images are presented in Fig. 11, with the initial and final periods of the build (duration 100 s) magnified for clarity.

In Fig. 10d, h_{scan} was obtained using a 3D scanner (Sect. 3.1), h_{cal} was obtained from y_{centre} ’s features as extracted from the height monitoring system presented here, and h_{ref} was obtained using the preprogrammed Δz and layer number. The data analysis for h_{scan} , h_{cal} , and h_{ref} follows the same logic as described for the triangle-shaped wall in Sect. 3.1 and Fig. 8d, e. h_{cal} and h_{scan} show good agreement, whereas h_{cal} and h_{ref} show relatively high differences, mainly at the corners of the build. The relative differences (δ) between h_{cal} and the other profiles are presented in Fig. 10e, and the resulting error measures values are presented in Table 3.

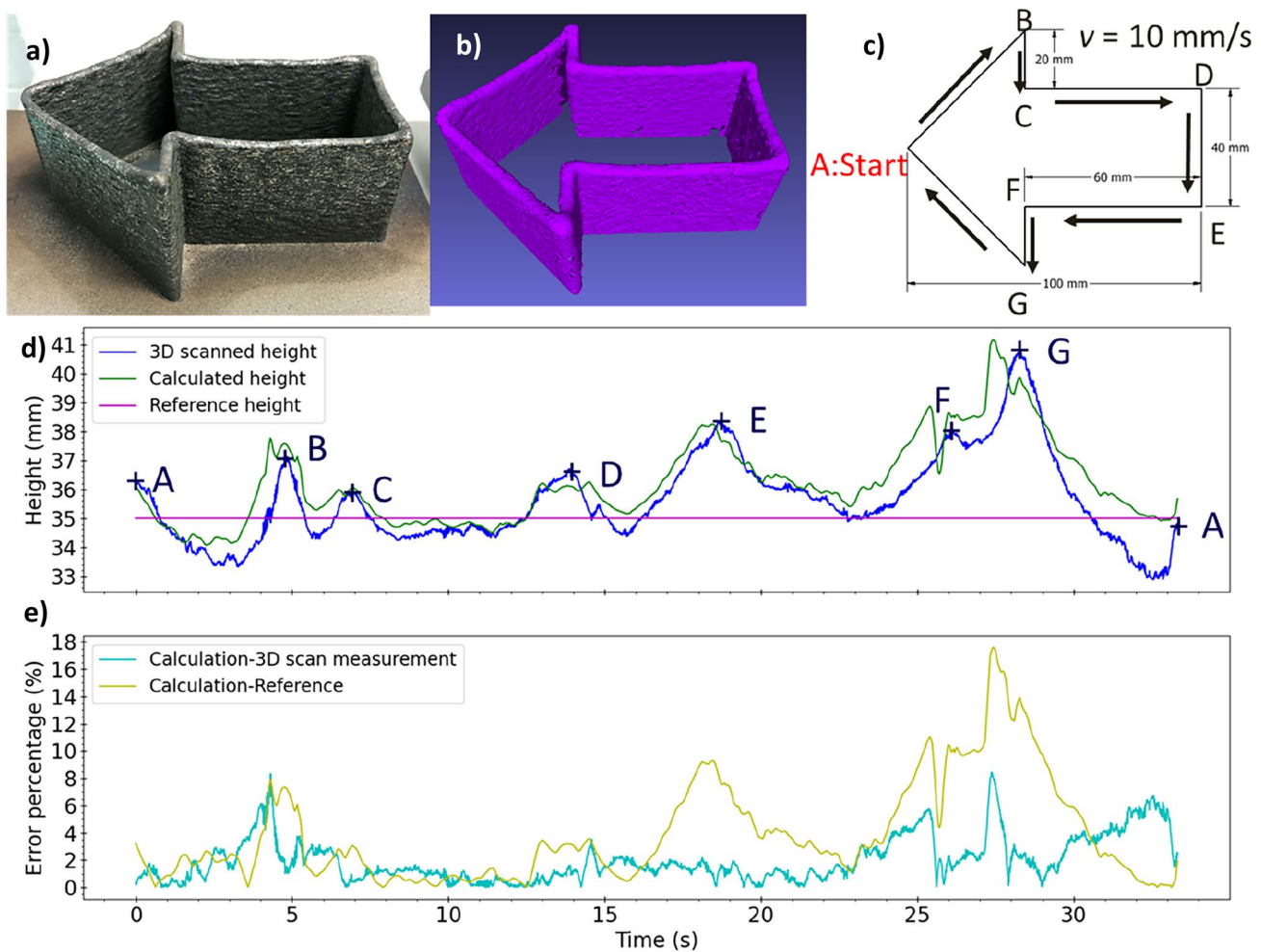


Fig. 10 Results for an arrow-shaped thin wall build. **a** Photograph of the completed build. **b** Surface of build obtained offline via a 3D scanner. **c** Plan view of the tool path used by the laser’s robotic arm, where v is the robot’s speed. **d** Comparison between the 3D-scanned

height (h_{scan}), calculated height (h_{cal} via Eq. (1)), and design height (h_{ref} , Sect. 3.1). The heights of positions A–G for the completed build are marked with blue crosses. **e** Discrepancy percentages for h_{cal} relative to h_{scan} , and h_{cal} relative to h_{ref}

Table 3 demonstrates that the MAE and MXAE between h_{cal} and h_{ref} are 1.36 mm and 6.16 mm, respectively, with the MXAE occurring at position G and leading to a relatively high MXAPE (17.59%). The MAE between h_{cal} and h_{scan} is 0.71 mm, which is relatively small and demonstrates the feasibility of the height monitoring method presented here. The MXAE and MXAPE are 3.2 mm and 8.44%, respectively, which are also reasonably low. As for the triangle-shaped wall build (Table 2), the relatively high MXAEs and MXAPEs appear mainly at the corners, where the build is also higher than the mid-sides, as seen for the triangle build (Fig. 8d). Also noteworthy is that the arrow build is more asymmetric around its symmetry plane than the triangle build. The reasons for the higher corners than the mid-sides are the same as the triangle build due to the acceleration/deceleration of the robot and the accumulated heat. The high MXAE/MXAPE values at the corners can be caused by the quality of the melt pool image and the data interpolation method used in the present study, which causes a small relative shift between the peaks of the h_{cal} and h_{scan} profiles presented in Fig. 10d. The cause of the asymmetric height profile of the arrow build around its single vertical symmetry plane is believed to be the uneven surface of the substrate (note that the triangle and arrow builds were fabricated on different plates). The cause of this unevenness is likely due to residual stresses, i.e. from when the substrate was cut into blocks from its originating steel sheet. Evidence for this uneven surface is presented in the Appendix.

4 Conclusions and future work

This study demonstrates the design and implementation of a low-cost, in situ monitoring system for measuring the built height online during the LMD process. The low-cost system comprised an off-axial webcam and bandpass filter (< USD\$1000). The built height was calculated based on the laser/powder defocusing distance and preprogrammed layer spacing. The former was obtained from the differential y-coordinates of the centre of the ellipse-fitted melt pool boundary. An adaptive thresholding method was presented to improve robustness that reduced the effects of the melt pool tail, which increases in length as heat accumulates with successive layers and thus would otherwise reduce the positioning accuracy of the melt pool centre.

The proposed height monitoring method was tested by fabricating two SS316L thin-wall builds (triangle shaped and arrow shaped). Both builds were 3D scanned offline using a portable 3D scanner to obtain their real overall height profiles. The calculated overall height based on the in situ monitoring system was compared with the 3D scanned overall height and the design height. The relative

difference between each pair of profiles was calculated and summarised using various error measures. Key results and conclusions are as follows:

- The built height can be acceptably precisely calculated based on the preprogrammed layer spacing and the differential y-coordinates of the centre of the ellipse-fitted melt pool, which was extracted from the presented in situ monitoring system. The system also proves the occurrence of laser/powder defocusing.
- The presented in situ monitoring system is highly sensitive to both height deviations in the build and the uneven surface of the substrate (see Appendix).
- The relatively high errors between the calculated height and design height usually appear at the build corners due to the deceleration of the laser and the resulting increase in heat input.
- The relatively high errors between the calculated height and the 3D scanned height usually appear at the corners. The cause relates to the method of melt pool extraction and the error introduced when interpolating the image data to a higher resolution.
- The MAEs between the calculated height and 3D scanned height for both builds are ~1 mm, with MAPEs < 5%. The MXAPEs between the calculated height and 3D scanned height for both builds are < 10%, comparable to the performance of state-of-the-art methods presented in the literature [14], but at a lower cost.

Despite the presented work providing reasonably accurate build height calculation, there are still several unaddressed aspects. (1) Image processing can be improved to extract a more accurate melt pool boundary location and thus further improve the accuracy of the calculated build height. (2) A cooling system would improve the camera's robustness over long build times. (3) The height monitoring system can monitor the built height in real-time non-intrusively. Thus, its output can be used as the measured signal to drive a feedback process control system to control build height for LMD systems, e.g. by adjusting the powder feed rate.

Appendix

A rapid flatness measurement was conducted to prove the hypothesis of the uneven surface of the mild steel substrate plate used for both builds described in this study. Figure 12a presents the tool path (plan view). Four points were selected near the corners. The pilot laser moved stepwise and clockwise along the path A-B-C-D-A. The video was recorded using the off-axial camera without the bandpass filter, as the pilot laser was working in the visible range. When the pilot laser reached the marked positions in Fig. 11a, the laser

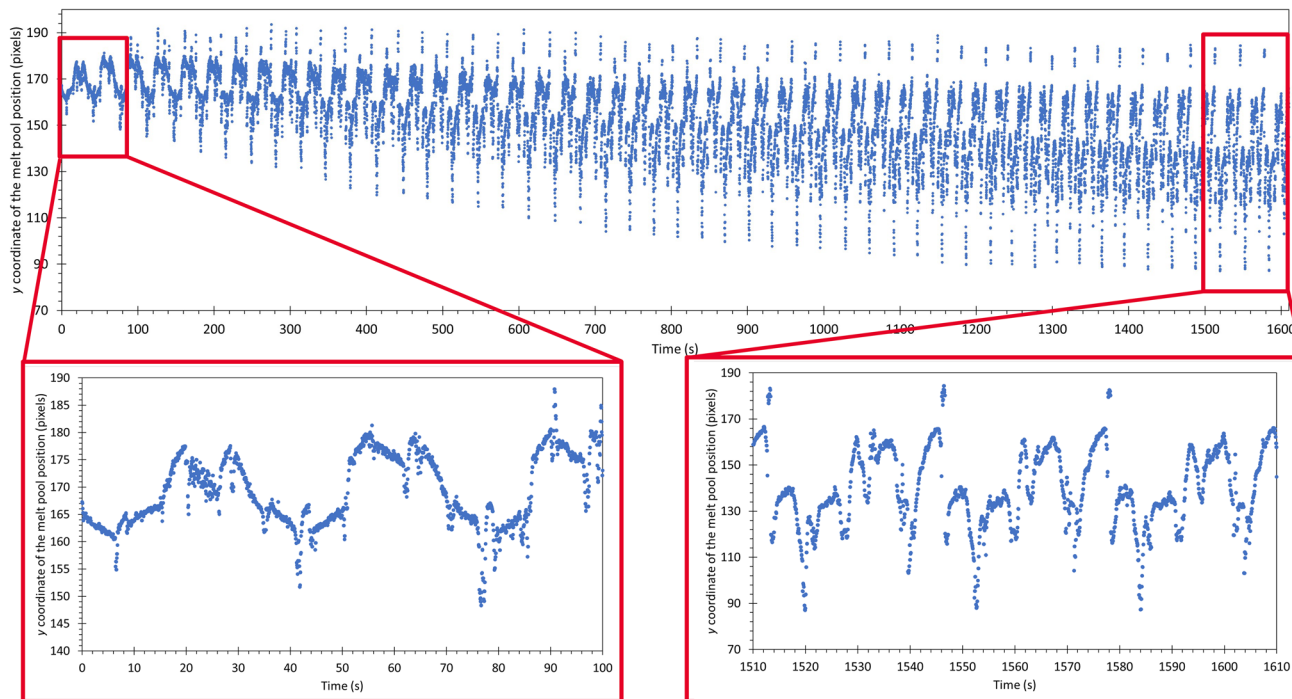


Fig. 11 y -coordinate of the melt pool centre (y_{centre}) as extracted from the melt pool images for the arrow-shaped thin wall build. The initial and final 100 s of the fabrication process are magnified for clarity

Table 3 Error measures between the calculated overall arrow-shaped thin wall height (after all image processing steps described in Sect. 2.4) and both the overall reference height and 3D scanned overall height. MAE and MXAE are precise to ± 0.01 mm, while MAPE and MXAPE are precise at 0.01%

Similarity of different height measures (\hat{h}, h)	MAE (mm)	MAPE (%)	MXAE (mm)	MXAPE (%)
h_{cal}, h_{ref}	1.36	3.88	6.16	17.59
h_{cal}, h_{scan}	0.71	2.00	3.20	8.44

head was stopped to measure the standoff distance between the nozzle end and substrate surface (~2-min process). Standoff distance was then manually measured using gauge-width leaves (Mitutoyo Corporation, Takatsuki, Kawasaki, Kanagawa, Japan) to ± 0.25 mm.

Data analysis requires a reference height, for which at point ‘A’ was selected. Figure 12b presents the comparison between flatness calculated from the off-axial camera video and direct measurements using the gauge leaves. Presented

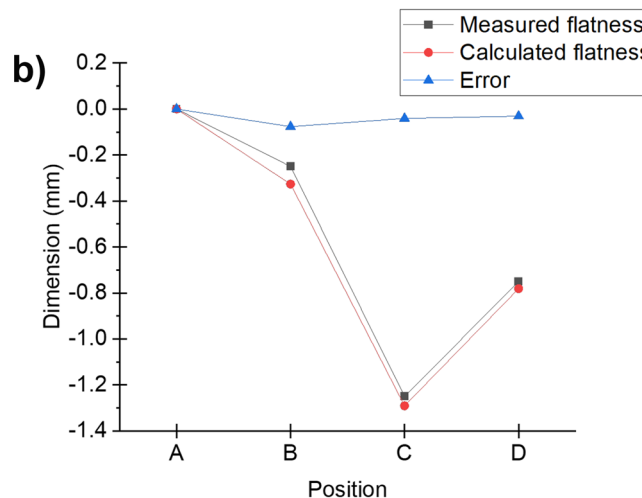
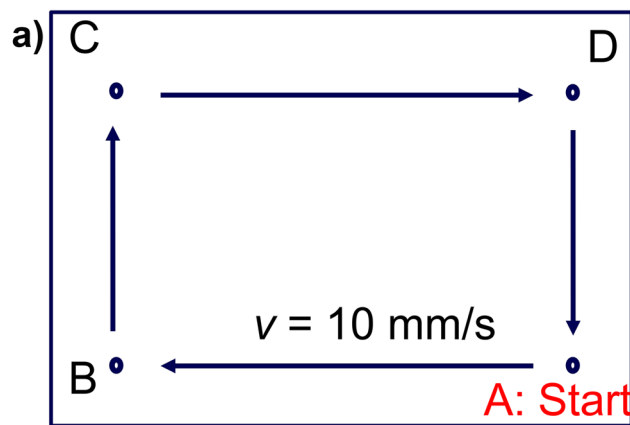


Fig. 12 a Tool path for flatness characterisation of the mild steel substrate plate used in this study (plan view). The pilot laser moved clockwise along A-B-C-D-A at speed v . **b** The comparison between

calculated flatness based on the off-axial camera images and direct measurements using gauge leaves is via the absolute error in calculated flatness

alongside is the resulting (small) error in flatness. These results demonstrate the resolution and robustness of the height monitoring system presented in this study. The results also show that B, C, and D lie below A, with C being the lowest point (~1.2 mm below A). Considering the size of the substrate plate ($150 \times 100 \times 10 \text{ mm}^3$), ~1 mm deviation in flatness is considered here to be acceptably small for the current purposes.

Acknowledgements The authors acknowledge the financial support provided by the Commonwealth Scientific and Industrial Research Organisation (CSIRO) and its Active Integrated Matter Future Science Platform (AIM FSP) [testbed no. AIM FSP_TB10_WP05]. The authors also acknowledge Hans Lohr (CSIRO) for his support with equipment purchase and configuration of the experimental setup, Teresa Kittel (CSIRO) for help with SEM (Fig. 3a), and Roshan Dodanwela (CSIRO) for help with 3D printing of the camera housing adaptor.

Author contribution Jiayu Ye, Nazmul Alam, Ivan Cole, and Reza Hoseinnezhad contributed to the study's conception and design. Data collection and analysis were performed by Jiayu Ye, Nazmul Alam, and Alireza Bab-Hadiashar. Contribution of knowledge was performed by Jiayu Ye, Nazmul Alam, Alejandro Vargas-Uscategui, Alireza Bab-Hadiashar, and Ivan Cole. The first draft of the manuscript was written by Jiayu Ye, and all authors commented on previous versions of the manuscript. All authors read and approved the final manuscript.

Funding Open Access funding enabled and organized by CAUL and its Member Institutions. This work was supported by the Commonwealth Scientific and Industrial Research Organisation (CSIRO) and its Active Integrated Matter Future Science Platform (AIM FSP) (testbed no. AIM FSP_TB10_WP05).

Data availability Not applicable.

Materials availability Not applicable.

Code availability Not applicable.

Declarations

Ethics approval Not applicable.

Consent to participate Not applicable.

Consent for publication Not applicable.

Competing interests The authors declare no competing interests.

Open Access This article is licensed under a Creative Commons Attribution 4.0 International License, which permits use, sharing, adaptation, distribution and reproduction in any medium or format, as long as you give appropriate credit to the original author(s) and the source, provide a link to the Creative Commons licence, and indicate if changes were made. The images or other third party material in this article are included in the article's Creative Commons licence, unless indicated otherwise in a credit line to the material. If material is not included in the article's Creative Commons licence and your intended use is not permitted by statutory regulation or exceeds the permitted use, you will need to obtain permission directly from the copyright holder. To view a copy of this licence, visit <http://creativecommons.org/licenses/by/4.0/>.

References

1. Wang X, Liu Z, Guo Z, Hu Y (2020) A fundamental investigation on three-dimensional laser material deposition of AISI316L stainless steel. *Opt Laser Technol* 126:106107. <https://doi.org/10.1016/j.optlastec.2020.106107>
2. Mukherjee T, DebRoy T (2019) A digital twin for rapid qualification of 3D printed metallic components. *Appl Mater Today* 14:59–65. <https://doi.org/10.1016/j.apmt.2018.11.003>
3. Chen M, Lu Y, Wang Z, Lan H, Sun G, Ni Z (2021) Melt pool evolution on inclined NV E690 steel plates during laser direct metal deposition. *Opt Laser Technol* 136:106745. <https://doi.org/10.1016/j.optlastec.2020.106745>
4. Garmendia I, Pujana J, Lamikiz A, Madarieta M, Leunda J (2019) Structured light-based height control for laser metal deposition. *J Manuf Process* 42:20–27. <https://doi.org/10.1016/j.jmapro.2019.04.018>
5. Zhu G, Li D, Zhang A, Pi G, Tang Y (2012) The influence of laser and powder defocusing characteristics on the surface quality in laser direct metal deposition. *Opt Laser Technol* 44(2):349–356. <https://doi.org/10.1016/j.optlastec.2011.07.013>
6. Sun J, Zhao Y, Yang L, Yu T (2019) Process optimization for improving topography quality and manufacturing accuracy of thin-walled cylinder direct laser fabrication. *Int J Adv Manuf Technol* 105(5–6):2087–2101. <https://doi.org/10.1007/s00170-019-04357-y>
7. Wang J-H, Han F-Z, Ying W-S (2019) Surface evenness control of laser solid formed thin-walled parts based on the mathematical model of the single cladding layer thickness. *J Laser Appl* 31(2):022009. <https://doi.org/10.2351/1.5067388>
8. Yu T, Sun J, Qu W, Zhao Y, Yang L (2018) Influences of z-axis increment and analyses of defects of AISI 316L stainless steel hollow thin-walled cylinder. *Int J Adv Manuf Technol* 97(5–8):2203–2220. <https://doi.org/10.1007/s00170-018-2083-x>
9. Sammons PM, Bristow DA, Landers RG (2019) Two-dimensional modeling and system identification of the laser metal deposition process. *J Dyn Syst Meas Contr* 141(2):021012. <https://doi.org/10.1115/1.4041444>
10. Garmendia I, Leunda J, Pujana J, Lamikiz A (2018) In-process height control during laser metal deposition based on structured light 3D scanning. *Procedia CIRP* 68:375–380. <https://doi.org/10.1016/j.procir.2017.12.098>
11. Tang L, Landers RG (2011) Layer-to-layer height control for laser metal deposition process. *J Manuf Sci Eng* 133(2):021009. <https://doi.org/10.1115/1.4003691>
12. Tan H, Chen Y, Feng Z, Hou W, Fan W, Lin X (2020) A real-time method to detect the deformation behavior during laser solid forming of thin-wall structure. *Metals* 10(4):508. <https://doi.org/10.3390/met10040508>
13. Asselin M, Toyserkani E, Iravani-Tabrizipour M, Khajepour A (2005) Development of trinocular CCD-based optical detector for real-time monitoring of laser cladding. *IEEE International Conference Mechatronics and Automation*, 2005, Niagara Falls, Ontario, Canada
14. Borovkov H, de la Yedra AG, Zurutuza X, Angulo X, Alvarez P, Pereira JC, Cortes F (2021) In-line height measurement technique for directed energy deposition processes. *J Manuf Mater Process* 5(3):85. <https://doi.org/10.3390/jmmp5030085>
15. Iravani-Tabrizipour M, Asselin M, Toyserkani E (2006) Development of an image-based feature tracking algorithm for real-time clad height detection. *IFAC Proc Vol* 39(16):914–920. <https://doi.org/10.3182/20060912-3-de-2911.00157>
16. Shi T, Shi J, Xia Z, Lu B, Shi S, Fu G (2020) Precise control of variable-height laser metal deposition using a height memory strategy. *J Manuf Process* 57:222–232. <https://doi.org/10.1016/j.jmapro.2020.05.026>

17. Song L, Bagavath-Singh V, Dutta B, Mazumder J (2011) Control of melt pool temperature and deposition height during direct metal deposition process. *Int J Adv Manuf Technol* 58(1–4):247–256. <https://doi.org/10.1007/s00170-011-3395-2>
18. Donadello S, Furlan V, Demir AG, Previtali B (2022) Interplay between powder catchment efficiency and layer height in self-stabilized laser metal deposition. *Opt Lasers Eng* 149:106817. <https://doi.org/10.1016/j.optlaseng.2021.106817>
19. Donadello S, Motta M, Demir AG, Previtali B (2019) Monitoring of laser metal deposition height by means of coaxial laser triangulation. *Opt Lasers Eng* 112:136–144. <https://doi.org/10.1016/j.optlaseng.2018.09.012>
20. Heralić A, Christiansson A-K, Lennartson B (2012) Height control of laser metal-wire deposition based on iterative learning control and 3D scanning. *Opt Lasers Eng* 50(9):1230–1241. <https://doi.org/10.1016/j.optlaseng.2012.03.016>
21. Microsoft LifeCam Cinema. Retrieved 15 Mar 2022 from https://www.centrecom.com.au/microsoft-lifecam-cinema?gclid=EAIaIQobChMIRk3tqt3v9AIVq5lmAh3JNQGjEAQYASABEGLC5_D_BwE
22. Bandpass Filter. Retrieved 15 Mar 2022 from <https://www.newport.com/p/20BPF10-900>
23. Repossini G, Laguzza V, Grasso M, Colosimo BM (2017) On the use of spatter signature for in-situ monitoring of laser powder bed fusion. *Addit Manuf* 16:35–48. <https://doi.org/10.1016/j.addma.2017.05.004>
24. Peng L, Shengqin J, Xiaoyan Z, Qianwu H, Weihao X (2007) Direct laser fabrication of thin-walled metal parts under open-loop control. *Int J Mach Tools Manuf* 47(6):996–1002. <https://doi.org/10.1016/j.ijmactools.2006.06.017>
25. OpenCV Bicubic Function (2021) Retrieved 7 Mar 2022 from https://docs.opencv.org/4.5.3/da/d54/group__imgproc__transform.html#enum-members
26. OpenCV Ellipse Fit Function (2021) Retrieved 7 Mar 2022 from https://docs.opencv.org/4.5.3/d3/dc0/group__imgproc__shape.html#gaf259efaad93098103d6c27b9e4900ffa
27. SciPy Interpolation Function (2022) Retrieved 7 Mar 2022 from <https://docs.scipy.org/doc/scipy/reference/interpolate.html>
28. Ikeuchi D, Vargas-Uscategui A, Wu X, King PC (2019) Neural network modelling of track profile in cold spray additive manufacturing. *Materials* 12(17):2827. <https://doi.org/10.3390/ma12172827>

Publisher's Note Springer Nature remains neutral with regard to jurisdictional claims in published maps and institutional affiliations.